Catalysis Science & Technology

ROYAL SOCIETY OF CHEMISTRY

PAPER

View Article Online
View Journal | View Issue

Cite this: *Catal. Sci. Technol.*, 2024, **14**, 5266

CO oxidation over a ligand coordinated single site Rh catalyst: identification of the active complex†

Fereshteh Rezvani, ‡[a] Xuemei Zhou, ‡[ab] Debora Motta Meira,[c] George E. Sterbinsky[d] and Steven L. Tait *[a]

Received 19th April 2024,
Accepted 25th July 2024

DOI: 10.1039/d4cy00507d

rsc.li/catalysis

Single atom catalysis has evolved as a promising strategy to enhance atom utilization efficiency, lower reaction temperatures, and control reaction pathways in heterogeneous catalytic reactions. An important challenge using supported single atom catalysts is the stability of metal single atoms during reactions. Here, we present an approach to stabilize single rhodium atoms on a titania support *via* a metal–ligand coordination strategy. We explore the reaction activity and mechanism of CO oxidation, as well as the stability under oxidative reaction conditions. Kinetic studies suggest that, with an excess of oxygen in the feed gas, oxygen activation is more facile on defective titania surfaces than on pristine titania surfaces. *In situ* diffuse reflectance infrared Fourier transform spectroscopy (DRIFTS) analysis shows that on the pristine titania surface, the 1,10-phenanthroline-5,6-dione (PDO) coordinated Rh catalyst (Rh–PDO/TiO_2) catalyzes CO oxidation *via* the formation of carbonate-like species, which is similar to what occurs on Rh nanoparticle catalysts. However, on the defective titania surface, no carbonate species form for Rh–PDO/def-TiO_2. The supported Rh–ligand catalysts are also shown to be very stable in such a reaction environment at elevated temperatures, potentially allowing for wide applications.

1. Introduction

The oxidation of carbon monoxide (CO) plays a crucial role in eliminating CO from gas streams, for instance, in automotive emission control and the purification of hydrogen fuel cell feeds. This reaction, one of the earliest[1] and most extensively studied heterogeneous reactions, can be catalyzed by noble metal catalysts in the form of supported metal particles, metal single atom catalysts (SACs), or metal single crystals in ultra high vacuum (UHV) conditions. While noble metal catalysts investigated over the years are dominated by Au, Pt, and Pd,[2–8] less attention has been directed to Rh. Supported Rh catalysts have shown to be promising for use in the CO oxidation reaction once the cost of Rh can be significantly decreased.[9,10]

The study of SACs for the CO oxidation reaction dates back to 2011, when one of the first studies demonstrated that a single atom Pt catalyst supported on FeO_x could catalyze CO oxidation at a relatively low temperature.[7] In their study, the single Pt atoms exhibited efficient atom utilization and strong interactions with the support. It has been reported that the support impacts the activity of metal centers through mechanisms such as strong metal–support interaction (SMSI) between metals and TiO_2 (ref. 11 and 12) or by varying the defect density in TiO_2 supports for Pt single atoms in hydrosilylation reactions.[13] Jiang *et al.*[14] showed that the presence of TiO_x species significantly improves the stability of the Pt–TiO_x–Al_2O_3 catalyst. This improvement is attributed to negative charge transfer from TiO_x to Pt, leading to less propylene adsorption on Pt sites and thus avoiding further dehydrogenation and hydrogenolysis in their study of propane dehydrogenation.[14] In the CO oxidation reaction, the activity of Pt_7 clusters is higher on a slightly reduced TiO_2 (110) surface than on a highly reduced surface.[5] The Ti^{3+} species at high concentration (highly reduced surface) will diffuse from the interstitial positions in the bulk to the surface and deplete adsorbed oxygen.[5]

Li's group reports that the reaction rate of CO oxidation for single Au atoms on defective TiO_2 is higher than that of Au on pristine TiO_2 at the same reaction temperature.[15] For Au on a defective TiO_2 surface, competitive adsorption is easier, and the energy barrier for CO oxidation is lower compared to Au on a pristine TiO_2 surface. However, this promotion is not sustained in oxygen-rich (near stoichiometric oxygen) conditions because the oxygen vacancies heal in seconds. The Ti–Au–Ti bond

[a] *Department of Chemistry, Indiana University, 800 E. Kirkwood Ave., Bloomington, Indiana 47405, USA. E-mail: tait@indiana.edu*
[b] *School of Chemical Engineering, Sichuan University, No. 24 South Section 1, Yihuan Road, Chengdu, 610065, P.R. China*
[c] *Canadian Light Source, Saskatoon, Saskatchewan, Canada*
[d] *Advanced Photon Source, Argonne National Laboratory, 9700 South Cass Avenue, Lemont, Illinois 60439, USA*

† Electronic supplementary information (ESI) available. See DOI: https://doi.org/10.1039/d4cy00507d

‡ These authors contributed equally to this publication.

structure on the defective surface could alleviate the competition in the adsorption of CO and O_2 on a single atomic Au site.[15] The Mars–van Krevelen (MvK) mechanism is related to the oxygen vacancy (O_v) formation energy of different oxide supports,[16] but the reaction in this work does not follow the MvK mechanism because the energy barrier is higher for CO molecules reacting with surface lattice oxygen compared to CO molecules reacting with adsorbed molecular oxygen.[15]

Over the years, investigations on Rh-based catalysts for CO oxidation have not significantly developed, and even less has been done on the corresponding reaction mechanism. Only a few studies have used *in situ* spectroscopy to engineer Rh single atoms on TiO_2.[17] A MvK mechanism is proposed in the case of Rh single atoms supported on a reducible support, such as heteropolyacid[16] or ceria.[10] In general, several mechanisms have been proposed for the CO oxidation reaction, including Langmuir–Hinshelwood (LH), Eley–Rideal (ER), and MvK. In the LH mechanism, CO and O_2 molecules are first co-adsorbed and then react to form an OOCO intermediate, which is the rate-determining step for the oxidation progress. In the ER mechanism, the activated O_2 molecules, as O atoms, directly react with free CO molecule from the gas phase, where the activation of O_2 is the rate-determining step. In the MvK mechanism, the CO reacts with lattice oxygen from the support to form CO_2, and subsequently, molecular O_2 replenishes the oxygen to the support.[18,19]

In this work, we adopted the metal–ligand approach that has been reported previously by our group to synthesize single site Rh on TiO_2 (Fig. 1).[20] The oxygen defects were introduced on the oxide support before the Rh–ligand loading. These defects play a role in the assembly of Rh with the ligand during deposition. The experiment will be performed under oxygen-rich reaction conditions, similar to those in current internal combustion engines (high air/fuel ratio) and catalytic converters. Hence, it is essential to investigate the reaction under oxidative conditions. In our previous work, we found that ligands coordinated to Pt kept Pt resistant to the reductive conditions.[21] However, the stability of metal–ligand catalysts under oxidative reaction atmospheres is not clear. In addition, the reaction serves as an ideal model reaction to investigate the reaction mechanism and identify active sites since it involves molecular rearrangements with CO- and oxygen-intermediates. Here, the Rh–ligand coordination of the catalyst will be resolved, and the active sites for the reaction will be identified using *in situ* spectroscopic and microscopic tools. The study of active sites under *in situ* conditions remains one of the essential challenges in heterogeneous catalysis.

2. Experimental section

2.1 Materials and chemical reagents

Titanium(IV) oxide (anatase, nanopowder, <25 nm, 99.7% trace metals basis), Rh(III) chloride hydrate (Rh 38–40%), 1-butanol (99.9%), 1,10-phenanthroline-5,6-dione (PDO, 97%), 3,6-di(2-pyridyl)-1,2,4,5-tetrazine (DPTZ, 96%), and 2,2′-bipyridine-5,5′-dicarboxylic acid (BPDCA, 97%) were purchased from Sigma-Aldrich. Dimethyl sulfoxide (DMSO, 99.90%) was purchased from Fisher Chemical. All chemicals were used without further purification. Compressed oxygen (UN 1072), ultra-high pure argon, carbon monoxide, and carbon dioxide were purchased from Airgas.

2.2 The preparation of Rh–ligand catalysts on titania by a modified wet-impregnation method

Titania (TiO_2) was used as the catalyst support, either in its pristine form (as received) or after an annealing treatment at a specific temperature to generate surface defects, particularly oxygen vacancies (O_v). This treatment, extensively explained in our previous work,[13] involved the characterization of Ti^{3+}/O_v states in the annealed TiO_2 using continuous wave (CW) electron paramagnetic resonance (EPR) spectroscopy (Fig. S1†), which is a widely employed technique for examining paramagnetic centers. For the annealed TiO_2 supports, 0.4 g TiO_2 powder was loaded into a ceramic crucible and placed in the center of a tube furnace. The tube furnace was first purged with pure lab nitrogen gas (99.998%, <3 ppm H_2O, <5 ppm O_2) for 30 min. Then, a flow of forming gas (5 vol% hydrogen, balanced in nitrogen gas, Airgas, 99.99%) at 2 L h^{-1} was started. Under this gas flow, the temperature was increased from room temperature to 500 °C at a ramp rate of 10 °C min^{-1}. After holding at this temperature for 1 h, the furnace was cooled down to room temperature in the forming gas flow.

The synthesis of titania supported Rh–ligand single atom catalysts is based on a modified wet impregnation method previously reported by our group.[20] To synthesize Rh–PDO on TiO_2, 0.3 g TiO_2 powder (pristine or annealed) was dispersed in 15 mL deionized (DI) water, sonicated for 5 minutes, and then stirred for 30 minutes. 0.0198 g PDO powder was dissolved in 15 mL DI water to form a yellow transparent solution and added to the dispersed TiO_2 under stirring. $RhCl_3$ aqueous solution was then added dropwise to the PDO/TiO_2/DI water mixture under stirring, aiming for a nominal Rh loading of 1.0 wt% and a molar ratio of Rh to PDO of 1:6. A Rh:PDO molar ratio of 1:9 was also synthesized but found to have poor metal loading (Table S1†)

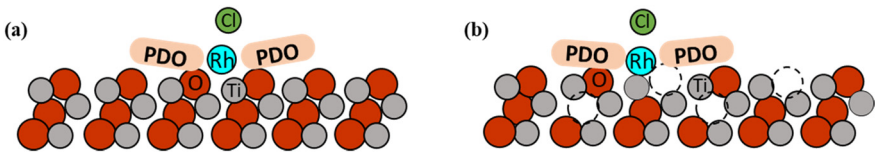

Fig. 1 Simplified schematic illustrations of Rh–PDO on (a) pristine TiO_2 and (b) defective TiO_2 with oxygen vacancies shown as dashed black circles.

and catalytic performance (Fig. S2†). The entire solution was kept at room temperature and stirred overnight. The synthesis of Rh–DPTZ and Rh–BPDCA on TiO_2 followed a similar process using 1-butanol as a solvent for DPTZ and $RhCl_3$ precursor and DMSO for BPDCA. The molar ratios of Rh : DPTZ and Rh : BPDCA were ideally calculated to be 1 : 3 with a nominal Rh loading of 1.0 wt%. After overnight stirring, the suspension was dried in an air stream, and the resulting precipitate was collected, washed with DI water, and finally dried in air. Rh/TiO_2 (without ligand) was prepared by adding $RhCl_3$ precursor into a TiO_2 suspension with 1 mL of 0.1 M NaOH, aiming for a nominal Rh loading of 2.0 wt%. After preparation, the solution was dried at 100 °C in air and washed with DI water. The Rh NPs were obtained by reducing the Rh/TiO_2 sample in Ar/H_2 (50% H_2) at 400 °C for 3 h before the CO oxidation reaction. Throughout this paper, we will use "TiO_2" to refer to the as-received TiO_2 powder and "def-TiO_2" to refer to TiO_2 powder annealed under forming gas at 500 °C. The chemical structures of the PDO, DPTZ, and BPDCA ligands are shown in Fig. 2a–c, respectively.

2.3 Characterizations of the as-prepared catalysts

X-ray Photoelectron Spectroscopy (XPS) measurements were conducted using a PHI Versaprobe II XP spectrometer, with a monochromated Al X-ray source, located at the Indiana University (IU) Nanoscale Characterization Facility (NCF). Rh 3d, Ti 2p, N 1s, C 1s, O 1s, and Cl 2p regions were collected. The binding energy of each spectrum was calibrated to the C 1s peak (284.8 eV). The intensity of each spectrum was normalized to that of the Ti 2p spectrum. XPS peak fitting was performed using CasaXPS software.

Scanning Transmission Electron Microscopy (STEM) imaging was carried out using a JEOL JEM NEOARM and JEOL JEM 3200FS microscopes, at the Indiana University Electron Microscopy Center. Energy dispersive X-ray spectroscopy (EDX) was used to analyze the quantity of each element, and the data were collected using the accessory of the same microscope.

Inductively Coupled Plasma Mass Spectrometry (ICP-MS) measurements were conducted using an Agilent 7700 quadrupole ICP-MS instrument, at the IU Department of Earth & Atmospheric Sciences. All solid catalysts were treated in *aqua regia* solution at 60 °C to dissolve all Rh, and the resulting solutions were analyzed after centrifugation and dilution. The calibration curve for Rh is performed using Rh standard for ICP (Sigma-Aldrich, in HCl) diluted with trace-free HCl for different concentrations.

X-ray Absorption Spectroscopy (XAS) was measured at the Rh K-edge, from 23 025 to 24 460 eV. The spectra consist of two main regions: the X-ray absorption near edge structure (XANES), near the absorption edge, and the extended X-ray absorption fine structure (EXAFS) region. The XAS measurements were performed at the 20-BM beamline at the Advanced Photon Source (APS) of Argonne National Laboratory using a double crystal Si (111) monochromator. The energy scale of the monochromator was calibrated using a Rh metal foil at the Rh K-edge. For all experiments, both fluorescence and transmission data were collected, and fluorescence data were used for analysis due to a better signal-to-noise ratio. Solid sample powder was pressed into a 7 mm diameter pellet and fixed to a mobile sample holder. Rh foil and Rh_2O_3 were used as standard samples for the XAS measurement (samples provided by the APS).

Analysis of the EXAFS data was carried out using the software ATHENA (part of the IFEFFIT package), including data alignment, edge calibration, deglitching, data normalization, and background subtraction. Fitting of EXAFS spectra was performed using ARTEMIS.[22] The EXAFS spectra were Fourier transformed after application of a Hanning window with a minimum k of 3.0 $Å^{-1}$, a maximum k between 13.4 and 15.0 $Å^{-1}$, and with a transition region of dk = 1.0 $Å^{-1}$. The Fourier transform range for each specific sample was selected based on the signal to noise ratio at high k and is given in Table S2.† Fitting of the Fourier transform was carried out over an R range from 1 to 3 Å. The amplitude reduction factor, S_0^2, and the energy shift between the measured and the theoretical spectra (ΔE_0) were abstracted from the fitting of standards (Table S2†).

CO adsorption was performed using Diffuse Reflectance Infrared Fourier Transform Spectroscopy (DRIFTS) at 30 °C under a 1 bar atmosphere. The DRIFTS cell was first purged with an Ar stream, followed by exposure to a CO/Ar mixture (CO 10%) for 10 min. After that, physically adsorbed CO was removed by flowing Ar (40 sccm) for 10 min. The background spectrum was collected after the Ar purge and before the addition of CO/Ar gas. *In situ* DRIFTS experiments were performed under Ar/O_2 (30 sccm/10 sccm), or Ar/CO (36 sccm/4 sccm) conditions, reflecting the feed gas conditions for CO oxidation in the fixed-bed reactor, to reveal the intermediates under reaction conditions. Each of the mass flow controllers

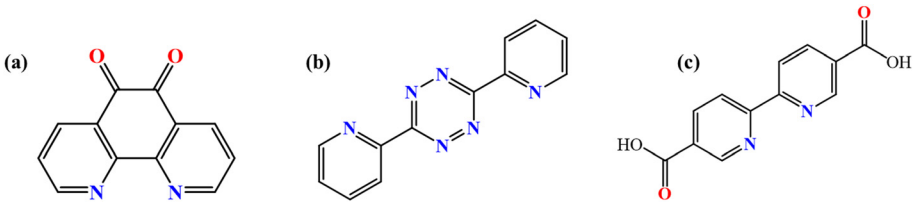

Fig. 2 Molecular structure of (a) 1,10-phenanthroline-5,6-dione (PDO), (b) 3,6-di(2-pyridyl)-1,2,4,5-tetrazine (DPTZ), and (c) 2,2′-bipyridine-5,5′-dicarboxylic acid (BPDCA).

was operated at standard temperature (25 °C), regardless of the reactor temperature, thus, flow rates are reported in units of standard cubic centimeters per minute (sccm). The background spectrum for the *in situ* DRIFTS was collected after the adsorption of CO at 30 °C. For the characterization of the surface functional groups, IR spectroscopy was performed with a diffuse reflectance IR environmental chamber (PIKE Technologies, 162-4160, HTV) at room temperature under flowing air. The Background spectrum was collected with pristine TiO_2. Each IR spectrum was an average of 500 scans and was converted into Kubelka–Munk units.

2.4 The catalytic testing of supported Rh–ligand catalysts

The CO oxidation reaction in the fixed-bed reactor was performed using a gas phase mixture of carbon monoxide and oxygen in a 1 : 25 ratio, balanced in Ar, with a flow ratio of 1% CO: 25% O_2: 74% Ar. The Rh–ligand catalyst loading was 100 mg in a quartz tube. The two ends of the catalyst bed were fixed with glass wool. The total height of the catalyst bed was approximately 1 cm, and the inner diameter of the quartz tube was 4 mm. The quartz tube containing the catalyst was covered with a thermal jacket. A K-type thermocouple was placed from the bottom of the tube, contacting the catalyst bed, and the gas mixture flowed from the top of the tube. Reactants and products were detected using a mass spectrometer. Fragments at m/z 28 (CO), 32 (O_2), and 44 (CO_2), were analyzed while the background was subtracted by flowing Ar/O_2 at a 75 : 25 ratio using an empty tube. The temperature of the catalyst bed was controlled by a temperature program, increasing from 30 °C to 200 °C in 10 °C intervals with a ramping rate of 1 °C min^{-1}. At each temperature, the reaction was held for 20 minutes. The CO conversion (X_{CO}) was calculated by comparing the CO concentration in the post-reactor gas flow during the reaction to the concentration when the reaction was not running, according to the following equation:

$$X_{CO} = \frac{[CO]_{feed} - [CO]_{product}}{[CO]_{feed}} \times 100\%$$

3. Results and discussion

3.1 Identification of the as-synthesized Rh–ligand catalysts

The synthesis of each Rh–ligand catalyst follows a modified wet impregnation method that has been reported previously[20] and is described in detail in the Experimental section.

The Rh 3d spectra (Fig. 3a) show a doublet for all the synthesized samples. The binding energy (BE) position of Rh suggests that the Rh in Rh–PDO coordination is charged, possibly at a 2+ chemical state.[23] For Rh–PDO on pristine TiO_2, the spectra are located at 308.2 eV and 313.0 eV for Rh $3d_{5/2}$ and $Rh3d_{3/2}$, respectively. On the defective TiO_2 surface, the BE positions of Rh in Rh–PDO assembly are similar to the former, as well as the full width at half maximum (FWHM) values, indicating similar Rh species in the two samples (FWHM = 2.5 eV).

However, for reduced Rh NPs on TiO_2, an additional doublet peak at a lower BE position is observed (307.2 eV for Rh $3d_{5/2}$ and 311.9 eV for $Rh3d_{3/2}$), which is ascribed to metallic Rh.[24] It is noted that under our reductive treatment conditions, the chemical state of Rh is not entirely rhodium zero; *i.e.*, partial Rh remains as Rh^{3+} from the precursor. The binding energy of such unreduced Rh is higher than that of Rh in the Rh–PDO ligand structure, indicating an electron transfer from the PDO ligand to Rh during coordination. The electron transfer between the PDO ligand and Rh can be observed from the N 1s spectra (Fig. 3b), where the peak position of N 1s for PDO deposited on TiO_2 (uncoordinated) is lower than that of PDO coordinated with Rh. Nevertheless, an insignificant amount of PDO adsorbs on pristine TiO_2 in the absence of Rh precursor. Cl 2p XP spectra are located at anion Cl^- positions (Fig. 3c). The Cl 2p intensity with PDO

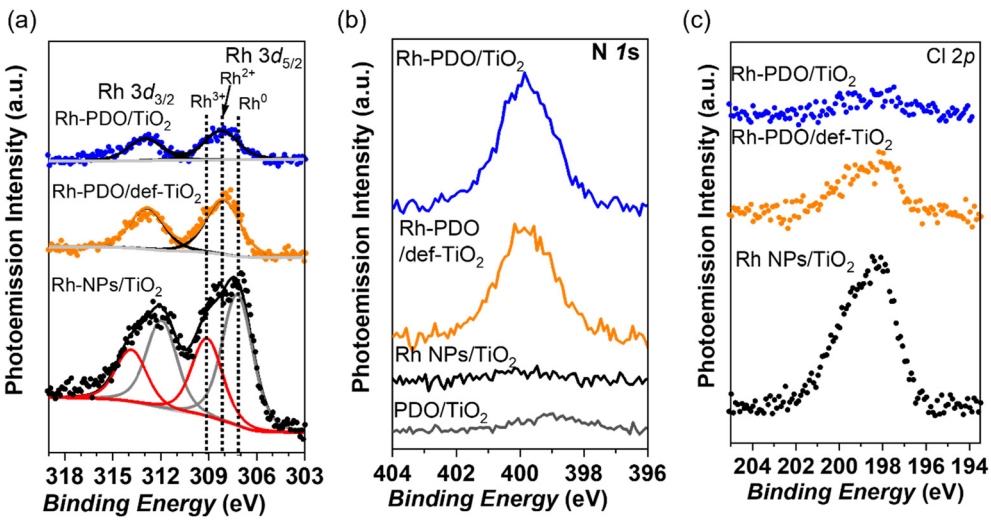

Fig. 3 XP spectra of (a) Rh 3d, (b) N 1s, and (c) Cl 2p for the Rh–PDO on pristine (blue curve) and on defective titania surface (yellow curve, def-TiO_2). The reduced Rh nanoparticles sample has been added for reference (black curve, bottom).

Table 1 Molar ratios of PDO/Rh, Rh/Ti, Cl/Rh, and PDO/Ti from XPS measurements on Rh–PDO/TiO_2, Rh–PDO/def-TiO_2, and Rh NPs/TiO_2. Rh wt% is measured from ICP-MS

Catalyst	XPS PDO/Rh mole ratio[a]	XPS Rh/Ti mole ratio	XPS Cl/Rh mole ratio	XPS PDO/Ti mole ratio	ICP Rh wt%
Rh–PDO/TiO_2	2.31	0.017	0.41	0.039	0.16
Rh–PDO/def-TiO_2	1.14	0.034	0.41	0.038	0.33
Rh NPs/TiO_2	N/A	0.096	0.73	N/A	0.70

[a] Calculated from XPS N 1s peak area and Rh 3d peak area.

presence is noticeably lower, possibly due to PDO replacement of Cl in the Rh coordination sphere. The above results show that the support surface has no significant impact on the oxidation state of Rh 3d, N 1s, and Cl 2p.

The elemental ratio of each element, based on the XP spectrum calculation, is presented in Table 1. The Rh/Ti ratio on the defective TiO_2 support is higher than that on a pristine surface, likely attributed to the higher concentration of surface defects offering more anchor sites for Rh. The Rh loading on the defective surface is twice the amount of that on the pristine surface, as measured by ICP-MS (Table 1). Moreover, Rh NPs/TiO_2 exhibit a higher Rh loading compared to the Rh–PDO/def-TiO_2 catalyst, as shown in Table 1 and Fig. 4c and f. The PDO/Rh ratio is 2.31 on the pristine surface and 1.14 on the defective surface, indicating that on the defective surface, Rh is less coordinated with the PDO ligand. Further coordination information has been revealed using EXAFS spectroscopy (Table S2†). The Cl/Rh ratios show a higher content of Cl on the Rh nanoparticles compared to that of Rh–PDO catalysts.

Infrared spectroscopy (Fig. S3†) confirms the successful deposition of the ligand (PDO) on Rh–PDO/def-TiO_2, as all PDO-derived features are observed. These features include ν(C═O) between 1710 cm^{-1} and 1720 cm^{-1}, aromatic overtones between 1800 cm^{-1} and 2000 cm^{-1}, ν(aromatic C═C) between 1500 cm^{-1} and 1600 cm^{-1}, and O–H/C–H bending (1455 cm^{-1} and 1000–1150 cm^{-1} for in-plane modes, 800–1000 cm^{-1} for out-of-plan modes).

3.2 The morphologies of as-prepared Rh–PDO catalysts and the dispersion of Rh nanoparticles

STEM images show the presence of Rh nanoparticles on the pristine titania support (Fig. 4a–c). These particles are measured to have an average diameter of 1.4 (± 0.2) nm. In the presence of the PDO ligand, the structure of Rh is significantly different that without the ligand, *i.e.*, hardly any evidence for Rh nanoparticle formation is observed in STEM imaging on either defective TiO_2 (Fig. 4d–f) or pristine TiO_2 (Fig. S4†).

In the characterization of metal single-atom catalysts, carbon monoxide is commonly employed as a gas probe molecule to assess the dispersion and oxidation state of the metal. In this study, we employ diffuse reflectance infrared Fourier transform spectroscopy (DRIFTS) to characterize the distribution of the Rh–ligand catalyst through CO adsorption.

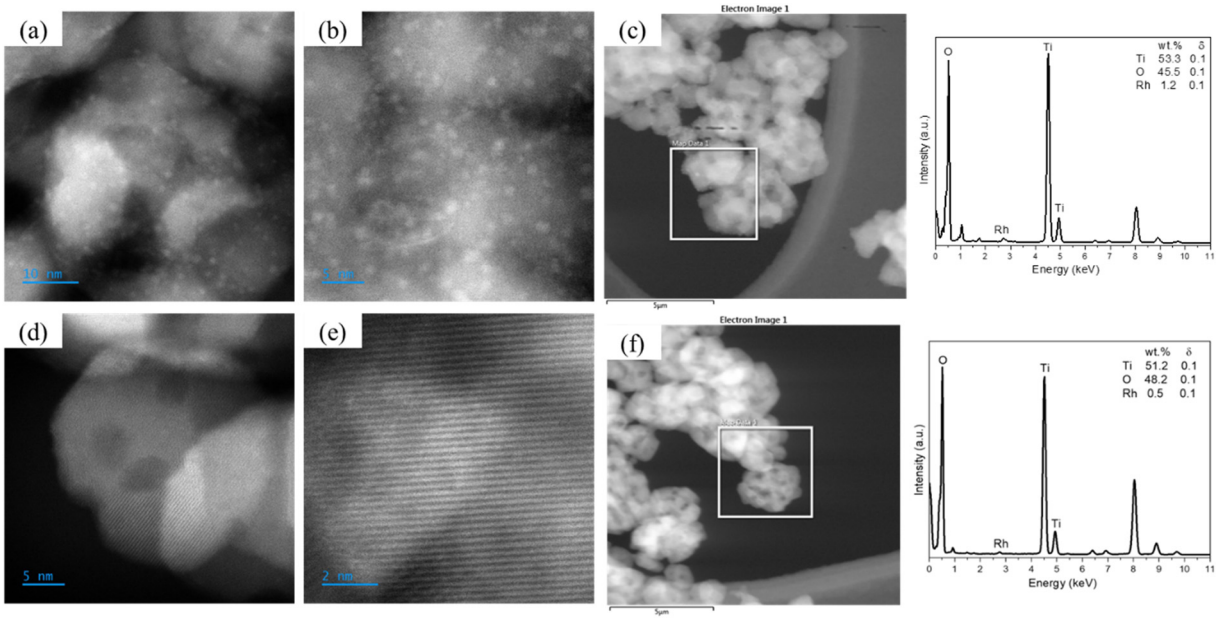

Fig. 4 STEM images of the (top row: a–c) supported Rh nanoparticles on pristine TiO_2 and (bottom row: d–f) the Rh–PDO/def-TiO_2. Corresponding EDX spectra are also presented in the same row. Fig. 4a, b, d and e were imaged with a JEOL JEM NEOARM microscope, while Fig. 4c and f, along with their respective EDX spectra, were acquired using a JEOL JEM 3200FS microscope.

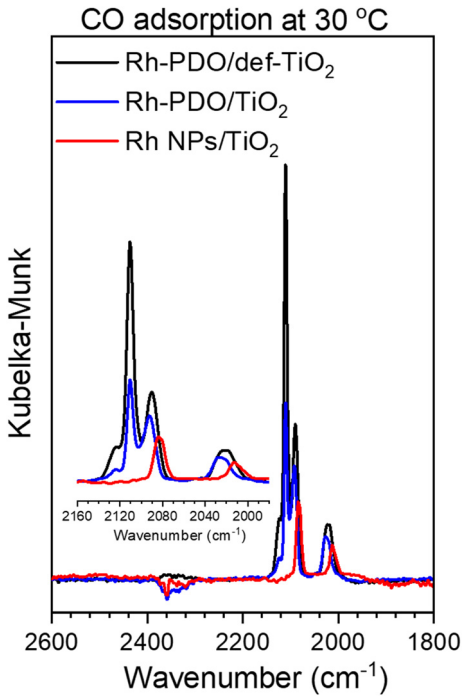

Fig. 5 CO adsorption spectra in DRIFTS at 30 °C at 1 atm on the Rh–PDO/TiO_2, Rh–PDO/def-TiO_2 and Rh NPs/TiO_2 (inset: enlarged region from 2160 cm^{-1} to 1980 cm^{-1}, showing the adsorption of CO vibrational bands). All spectra were collected after CO adsorption for 10 min and then Ar purging for 10 min to remove physically adsorbed CO.

In the reduced Rh NPs sample, two CO adsorption bands are observed: one located at a higher wavenumber of ~2084 cm^{-1} and the other at a lower wavenumber of ~2012 cm^{-1} (Fig. 5, red curve). These bands are ascribed to the *gem*-dicarbonyl species of $Rh^0(CO)_2$, corresponding to the symmetric and anti-symmetric CO-stretching modes, respectively.[25] The intensity ratio of the doublet is related to the angle between carbonyl groups.[17] However, there is a lack of a bridged CO band at 1860 cm^{-1}, as well as the linearly adsorbed CO on Rh_{NPs}^0 (2060–2070 cm^{-1}), indicating the absence of large/bulk metallic Rh species for Rh NPs.[26] This observation aligns with the Rh 3d XP spectrum (Fig. 3a), where a mixture of Rh^0 and Rh^{3+} is observed. It is possible that the Rh NPs exhibit a core–shell structure, with a core of Rh oxide on the oxide support and metallic Rh on the surface.

For Rh–PDO on the pristine surface, the doublet is located at relatively higher wavenumbers, approximately 2093 cm^{-1} and ~2025 cm^{-1}, compared to that on Rh NPs. This difference can be ascribed to the weaker back donation from the filled d orbital of Rh^{2+} to the anti-bonding orbital of CO compared to the d orbital of Rh^0. In the literature, the doublet of CO frequencies in Rh $(CO)_2^{3+}$ configuration is located at 2110 and 2039 cm^{-1},[17,27] indicating that Rh in the Rh–PDO structure is at 2+ chemical state. In addition, the CO adsorption doublets of Rh–PDO on defective titania are located at 2090 cm^{-1} and 2021 cm^{-1}, which are slightly lower than those on pristine titania.

More importantly, for both Rh–PDO samples, an additional peak at 2110 cm^{-1} is attributed to linearly adsorbed CO on the cationic Rh site.[28] The shoulder above the highest peak, located at 2124 cm^{-1}, is assigned as a third CO insertion into the $Rh^{2+}(CO)_2$.[26] Overall, the CO adsorption peak is more intensive on the defective surface than on the pristine surface (black curve, compared to the blue curve), indicating a higher density of CO adsorption sites on the Rh–PDO/def-TiO_2.

The Rh K-edge XANES reveals that the Rh in the Rh–PDO structure is oxidized on both the defective and pristine titania support (Fig. 6a), based on comparison to metallic Rh foil.

The reduced Rh nanoparticles on pristine TiO_2 are not entirely in the metallic state but remain partially oxidized. We note that XPS measurements also show that Rh is not exclusively in a metallic state; some Rh 3d signals correspond to an oxidized state (Fig. 3a). A potential reason for this incomplete reduction could be the sample treatment after Rh deposition. The sample underwent an annealing step in Ar/H_2 at 400 °C for 3 h, which may induce a strong metal support interaction (SMSI).[29] This interaction may result in the embedding of Rh particles in the oxide support and simultaneously creating vacancies on the support surface.[29] This process can act as a barrier, preventing some Rh particles from being fully reduced to the zero-oxidation state, thereby leaving a portion in an oxidized state.

The EXAFS spectrum for Rh NPs shows the presence of both Rh–O and Rh–Rh paths (Fig. 6b), resulting in an *N* (Rh–

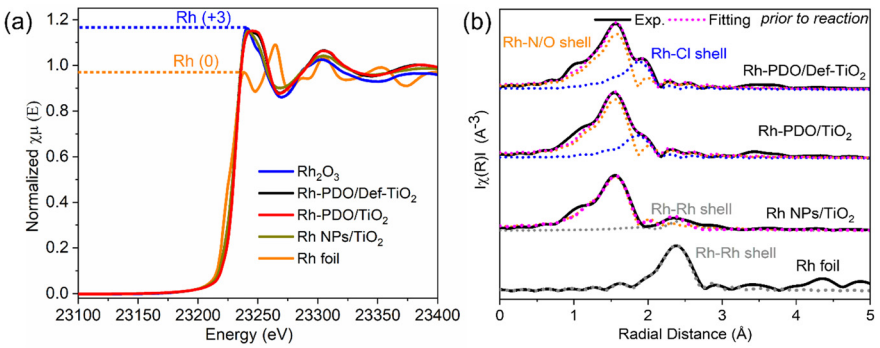

Fig. 6 (a) XANES and (b) k^2-weighted EXAFS spectra at the Rh K-edge for Rh–PDO on defective and pristine TiO_2, Rh NPs, and Rh_2O_3. The Rh foil sample was measured for reference.

Rh) of 1.7 and *N* (Rh–N/O) of 5.2 (Table S2†). The relatively low *N* (Rh–Rh) value, compared to metallic Rh on oxide supports in the literature,[30–32] may be ascribed to the incomplete reduction of Rh NPs or the very small particle size (Fig. 4a) observed in our samples, which may allow for significant Rh–O interaction. This value is also lower than that reported for Rh NPs on TiO_2 (0.5 wt%),[30] likely due to the high dispersion of Rh NPs and *ex situ* treatment conditions. More importantly, for the Rh–ligand catalysts, no Rh–Rh path is observed. The *N* (Rh–Cl) is 1.4 for Rh–PDO on defective TiO_2 and 1.0 for Rh–PDO/TiO_2. The *N* (Rh–N/O) is 4.8 for Rh–PDO on defective TiO_2 and 5.1 for Rh–PDO/TiO_2. Compared to the single site Rh on metal oxide in the literature,[10,17,33] the loading of single site Rh in our work is relatively high, indicating that the presence of the PDO ligand allows the high dispersion of Rh.

3.3 The catalytic performance of Rh–ligand catalysts

We further explore how the coordination of Rh affects the reaction pathway of CO oxidation by investigating the conversion of CO at different reaction temperatures. CO oxidation was tested in a fixed-bed flow reactor with a reaction gas composition of 1 vol% CO and 25 vol% O_2, balanced in Ar. We selected a high O_2/CO ratio in our experiments to achieve the so-called "hyperactive" states, that require an O_2/CO ratio > 10 for Rh metal, as reported in the literature.[34] Under stoichiometric O_2/CO conditions, the Rh surface will be essentially saturated with chemisorbed CO, resulting in far less activity for CO oxidation.[34]

The profiles of CO conversion as a function of reaction temperature upon heating (Fig. 7) for different Rh–ligand catalysts and a Rh NPs catalyst show distinct reaction paths. The CO conversion over Rh–PDO/def-TiO_2 exhibits an onset of CO oxidation reactivity at 70 °C and reaches 90% conversion by 190 °C. The T_{50} (50% conversion of CO) for this catalyst is 115 °C, which is significantly lower than that for Rh–PDO on pristine TiO_2 surface (183 °C), and for reduced Rh nanoparticles on TiO_2 (198 °C). The T_{50} for our best catalyst is comparable to the Rh_1/CeO_2 and lower than the T_{50} (150 °C) for the commercial three-way-catalyst.[10] Except for the phenanthroline dione ligand, we employed two other ligands: bipyridyl with dicarboxylic acid groups and tetrazine structure, to coordinate with Rh. These two catalysts (Rh–BPDCA and Rh–DPTZ) exhibited reluctance to convert CO in the examined temperature range, likely due to their very low Rh loading (Fig. 7a). Characterizations of the Rh–BPDCA and Rh–DPTZ catalysts are shown in the ESI† (Fig. S6 and S7, and Table S1).

At 140 °C, the performance of the catalyst remains stable for a certain period of reaction time (Fig. 7b). The CO conversion rate at the Rh site is calculated for each catalyst, and the results show that at 140 °C, the CO conversion rates are 2.15 mol g_{Rh}^{-1} h^{-1} for Rh–PDO/def-TiO_2, 1.23 mol g_{Rh}^{-1} h^{-1} for Rh–PDO/TiO_2, 0.15 mol g_{Rh}^{-1} h^{-1} for Rh NPs/TiO_2, 0.31 mol g_{Rh}^{-1} h^{-1} for Rh–DPTZ/def-TiO_2, and 0.15 mol g_{Rh}^{-1} h^{-1} for Rh–BPDCA/def-TiO_2. The atom utilization efficiency for Rh coordinated with the ligand is an order of magnitude higher than that in nanoparticles.

In addition, our results show no oxygen poisoning observed with Rh–ligand catalysts, even under oxygen-rich conditions (Fig. 7b). Therefore, from a fundamental perspective, it is important to study in detail the nature of the active surfaces for Pt-group metals in oxygen-rich conditions using *in situ* characterization techniques. Sautet *et al.*[33] demonstrated that single site Rh_1 can adapt to the environment using *in situ* STEM imaging combined with DRIFTS.

3.4 The evolution of CO at Rh sites under O_2-rich conditions: impact of support surface

To identify adsorbed CO species on both the Rh site and TiO_2 support during CO oxidation, *in situ* DRIFTS analyses were performed using Rh–ligand and Rh NPs/TiO_2 catalysts (Fig. 8).[33,35] In each experiment, the temperature was increased in 10% O_2 after CO adsorption at 30 °C.

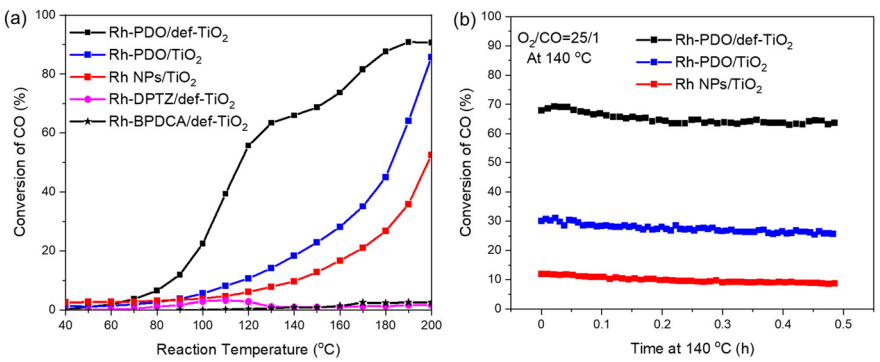

Fig. 7 (a) CO conversion as a function of reaction temperature over Rh–PDO on defective titania, and Rh–PDO on pristine titania, in comparison to the supported Rh NPs on pristine titania. Two catalysts of Rh coordinated with other ligands, namely Rh–BPDCA and Rh–DPTZ, are included for reference. (b) Conversion of CO at 140 °C. In each experiment, the mass of the catalyst loaded into the reactor was 100 mg, but the loading of Rh metal varies, with the Rh NPs catalyst having the largest metal content by at least a factor of 2 compared to the other catalysts (see Tables 1 and S1† for Rh wt% loading).

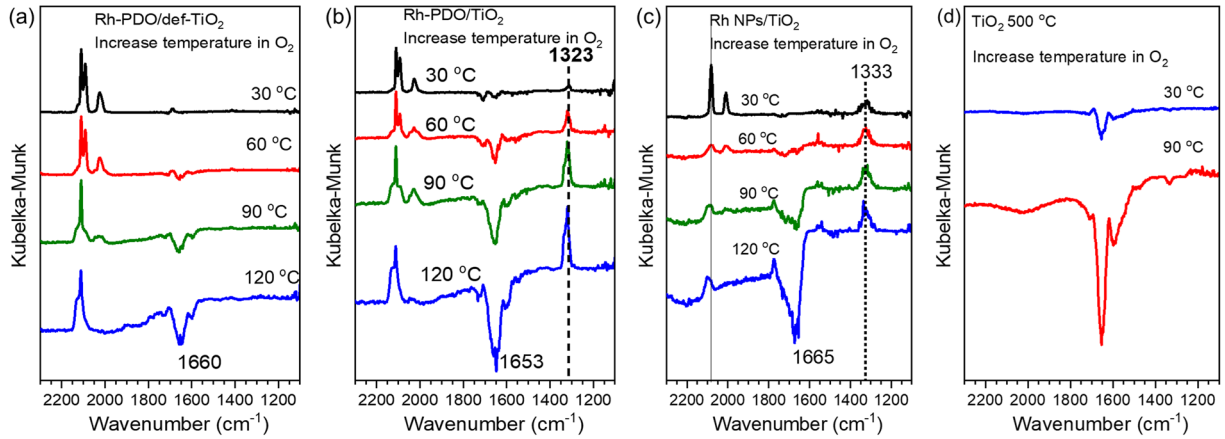

Fig. 8 DRIFT spectra for (a) Rh–PDO/def-TiO_2, (b) Rh–PDO/TiO_2, (c) Rh NPs/TiO_2, and (d) bare defective TiO_2 without Rh loading, at temperatures indicated with a 10 vol% oxygen flow balanced in Ar after CO adsorption at 30 °C (shown in Fig. 5). In (b) and (c), peaks at 1323 cm^{-1} and 1333 cm^{-1} are due to carbonate formation on the surface, which is essentially trapped on the surface under these oxygen flow conditions but could react away with CO under reaction conditions. Note that for Rh–PDO/def-TiO_2 (a), these peaks are not observed due to the desorption of the oxidation product as CO_2. The negative peak at ~1660 cm^{-1} is due to the loss of surface hydroxyl.

For Rh–PDO on defective TiO_2 (Fig. 8a), as the temperature rises, the intensity of *gem*-dicarbonyl CO in $Rh^{2+}(CO)_2$ (2090 cm^{-1}, 2021 cm^{-1}) significantly decreases when the temperature reaches 90 °C, completely vanishing at 120 °C. A gradual increase in the region around 1660 cm^{-1} is ascribed to the desorption of the bending vibration of coordinated H_2O as well as Ti–OH, which is also observed for the pure defective titania (Fig. 8d). Linearly adsorbed CO persists up to 120 °C, and a shoulder at a higher wavenumber (~2136 cm^{-1}) appears, attributed to Rh^{2+}–CO–O–O (a bridged O_2 on Rh^{2+}).[36] For Rh–PDO on a pristine TiO_2 surface (Fig. 8b), the evolution of CO molecules takes place differently. There is no clear decrease in the *gem*-dicarbonyl CO in $Rh^{2+}(CO)_2$ (~2093 cm^{-1} and ~2025 cm^{-1}) until 120 °C, which may explain the relatively high onset temperature in Fig. 7, as the strong adsorption of reactant molecules may hinder the subsequent heterogeneous reaction.

More predominantly, for Rh–PDO and Rh NPs on pristine surface, we observe an increase in the peak at ~1323 cm^{-1}, starting from 30 °C, which further increases significantly at 90 °C. This feature at FTIR has been ascribed to carbonate-like species on TiO_2,[37,38] originating from the product CO_2 further reacting with surface oxygen and forming carbonate species. It could be attributed to CO_3 in a bidentate binding position on the Ti site (ν_{SS} = 1330 cm^{-1} for asymmetric νCOO).[37] These species are not observed for Rh–PDO on defective TiO_2, which may result from the rapid desorption of the generated CO_2 from the surface. We attribute the difference in CO_2 desorption to the specific configuration of the Rh–ligand on the defective surface, which blocks the formation of carbonates.

For Rh NPs on TiO_2 (Fig. 8c), a clear decrease in the *gem*-dicarbonyl CO in $Rh^0(CO)_2$ (2084 cm^{-1}, 2012 cm^{-1}) indicates that the CO molecule was consumed/desorbed at 60 °C. However, it is likely that the CO molecules are converted to carbonate-like species on TiO_2, not to gas phase CO_2, as the peak intensity for carbonate-like species increases. Note that this catalyst was reduced in Ar/H_2 (50% H_2) at 400 °C for 3 h; considering the spillover effect of hydrogen onto the surface,[39] a strong metal support interaction may be introduced. Despite this, for this catalyst, below 120 °C, there is no plausible CO_2 generation. Above 90 °C, the CO adsorption changes from *gem*-dicarbonyl CO to a single CO adsorption band at 2100 cm^{-1}, which corresponds to linearly adsorbed CO on single cationic Rh. It is thus deduced that the supported Rh NPs catalyst experiences a different mechanism for CO oxidation reaction, which may need to overcome a higher energy barrier compared to Rh–PDO on defective TiO_2.

3.5 Thermodynamic analysis of the reaction pathway based on DRIFTS

While the literature indicates that, with reducible support, single site metal catalysts often undergo a Mars–van Krevelen mechanism for CO oxidation, exceptions exist.[10,40] It has been reported that, in the case of a single Rh atom on a ceria surface, the CO reacts with CeO_2 lattice oxygen *via* the Mars–van Krevelen mechanism, while Rh nanoparticles on CeO_2 follow a Langmuir–Hinshelwood mechanism.[10] Nevertheless, recent studies suggest that the Mars–van Krevelen CO oxidation mechanism is barely possible on single site Au/TiO_2 due to a higher energy barrier for CO reacting with lattice oxygen (2.73 eV of O_{2c} and 2.79 eV of O_{3c}). This is in contrast to the free energy of CO reacting with molecular oxygen species in air (0.6 eV of O_{2c} and 0.72 eV of O_{3c}).[15] The co-adsorption of CO and O_2 shows greater favorability on single site Au on a defective TiO_2 (001) compared to a defective TiO_2 surface (without Au).[15] Furthermore, under oxygen-rich conditions, the probability of participation of support oxygen is low.[41]

We conducted DRIFTS measurements for Rh NPs/TiO_2 in a pure Ar flow at elevated temperatures after CO adsorption at 30 °C (Fig. 9a). The results reveal no significant changes in the position of the CO adsorption bands, and any changes in peak shape can be due to variations in the background peak of

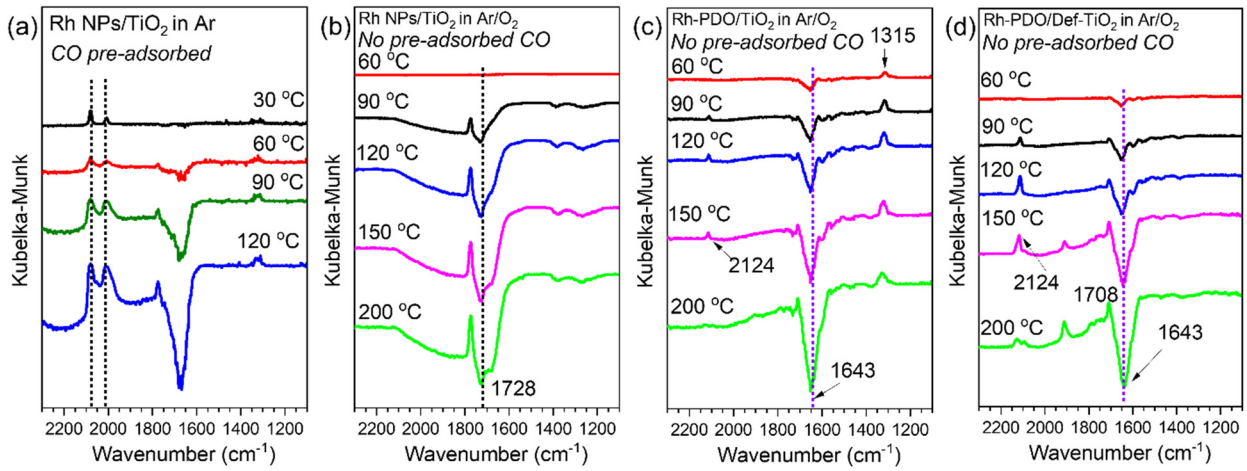

Fig. 9 (a) DRIFT spectra for Rh NPs/TiO_2 at elevated temperature under Ar (without oxygen) after CO adsorption at 30 °C. The evolution of catalysts with increasing temperature in Ar/O_2 (without CO) is shown in the DRIFT spectra for (b) Rh NPs/TiO_2, (c) Rh–PDO/TiO_2, and (d) Rh–PDO/def-TiO_2.

titania. Importantly, there is no obvious formation of carbonate-like species on the TiO_2 surface when there is no oxygen gas flow. Therefore, we can exclude the possibility of a Mars–van Krevelen mechanism (CO reaction with support oxygen) for Rh NPs/TiO_2. We were not able to conduct the same experiment for Rh–ligand catalysts, as these tend to aggregate at high temperatures (200 °C) in an Ar environment without oxygen.

However, to further elucidate the mechanism of carbonate species formation, we carried out DRIFTS experiments using Rh NPs/TiO_2, Rh–PDO/TiO_2, and Rh–PDO/def-TiO_2 without pre-adsorbed CO molecules (Fig. 9b–d). In each case, the background DRIFT spectra obtained at 30 °C was subtracted from the data. In Fig. 9b, without CO pre-adsorption, no carbonate-like species formation is observed at high temperatures, which further suggests that carbonates are generated during the CO oxidation reaction. Fig. 9c shows a weak intensity of the carbonate peak (1315 cm^{-1}) and the CO adsorption peak (2124 cm^{-1}) for Rh–PDO/TiO_2 (Fig. 9c), possibly indicating the oxidation of surface carbon species. For Rh–PDO/def-TiO_2 (Fig. 9d), only a weak CO adsorption peak is observed. However, according to the IR spectra of the fresh catalyst (Fig. S3†), it is evident that the carbonate does not originate from the catalyst ligand. Overall, the results in Fig. 9 supplement the findings in Fig. 8 indicating that carbonate formation occurs during CO oxidation for the less active two catalysts (Rh NPs/TiO_2 and Rh–PDO/TiO_2). However, for Rh–PDO/def-TiO_2, CO is converted to gaseous CO_2 at a relatively low temperature through a $Rh^{2+}(CO)_2$ intermediate.

3.6 Kinetic analysis of the reaction mechanism on ligand-coordinated single-site Rh

To further reveal the role of oxygen during the CO oxidation reaction, we performed kinetic measurements to determine the oxygen reaction order at different CO partial pressures (Fig. 10 and Table 2) at 140 °C. The kinetic study revealed reaction orders between 0–0.5 for oxygen in Rh NPs/TiO_2, 0.4–1.0 for Rh–PDO/def-TiO_2, and above 1 for Rh–PDO/TiO_2. A first-order dependence on O_2 at a fixed CO partial pressure indicates that oxygen activation is involved in the rate-determining step, while a zero-order dependence suggests facile O_2 activation. The reaction order of oxygen that we reported for the single site Rh–ligand catalyst is different from that of single site metals for CO

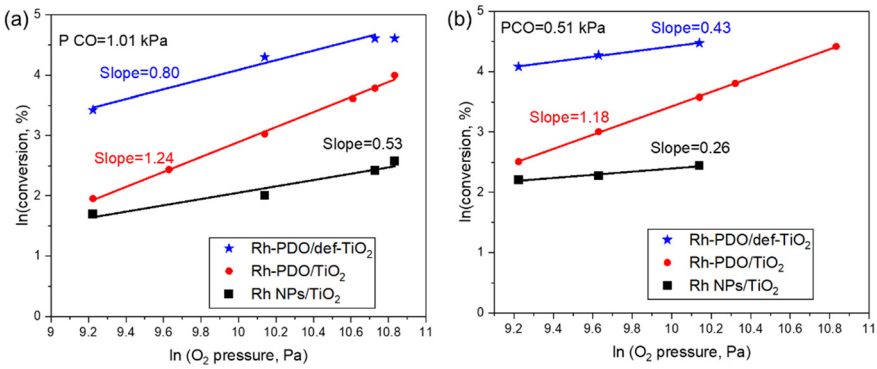

Fig. 10 Reaction orders for oxygen for the three catalysts at (a) P_{CO} = 1.01 kPa and (b) P_{CO} = 0.51 kPa.

Table 2 Reaction order for CO and O_2 at different partial pressures for the Rh–PDO ligand catalysts and supported Rh NPs. Note that at 140 °C, the conversions differ among the three samples

	O_2 reaction order	
	P_{CO} = 1.01 kPa	P_{CO} = 0.51 kPa
Catalysts	ln P = 6.9	ln P = 6.2
Rh–PDO/TiO_2	1.24 (9.2–10.9)	1.18 (9.2–10.9)
Rh–PDO/def-TiO_2	0.80 (9.2–10.7)	0.43 (9.2–10.2)
Rh NPs/TiO_2	0.53 (9.2–10.9)	0.26 (9.2–10.2)

oxidation,[10] possibly due to the oxygen-rich conditions applied in our experiments.

In our experimental setup, we observed that the oxygen dependence (around 1.2) of Rh–PDO/TiO_2 remains unaffected by variations in CO partial pressure. This suggests the exclusion of the competitive Langmuir–Hinshelwood mechanism. Instead, the reaction on Rh–PDO/TiO_2 may follow the Eley–Rideal mechanism. Despite the excess oxygen in this experiment, oxygen molecules participate in the reaction as intermediate states, either as single oxygen atoms, as two individual oxygen atoms, or bridged oxygen species.[36] However, for Rh NPs/TiO_2, the low oxygen reaction order indicates facile oxygen dissociation on Rh NPs. The oxygen dependence decreases (from 0.53 to 0.26) as the CO partial pressure drops (Fig. 10a and b), suggesting a competing Langmuir–Hinshelwood (L–H) mechanism.

In the case of Rh–PDO on defective TiO_2, a similar CO dependence and oxygen reaction order are observed, with the oxygen reaction order decreasing from 0.80 to 0.43 as the CO pressure decreases. Although the oxygen reaction order for single site Rh on defective support is 0.4–0.8, indicating a less facile oxygen activation process compared to Rh NPs, the kinetic analysis for this catalyst at 140 °C, which shows a CO conversion of about 70% (Fig. 7), falls beyond the rational region. However, DRIFTS results demonstrate that for Rh–PDO/def-TiO_2, the conversion of CO with oxygen generates gaseous CO_2 rather than carbonate intermediates, which significantly facilitates the reaction thermodynamically.

Therefore, kinetically, for the single-site Rh coordinated with PDO on the pristine TiO_2 support, the CO reaction may occur *via* an Eley–Rideal (E–R) mechanism, where CO coordinates with Rh, and the dissociated oxygen reacts with the coordinated CO molecule. In previous studies, it has been reported that supported Rh single atom catalysts follow the Mars–van Krevelen (MvK) mechanism for CO oxidation.[10,17,42] For instance, in a study conducted by Han, *et al.*,[10] the MvK mechanism was proposed based on CO-DRIFTS experiments and reaction rates as a function of CO and O_2 concentrations. We did not find other prior examples of supported Rh single atoms following the E–R mechanism; however, it may be useful to consider supported Ir single atoms, which are reported to follow the E–R mechanism. In a study by Lu, *et al.*,[40] it was found that the coordination ability of Ir single atoms to multiple ligands allows the CO molecule to coordinate at the Ir site, forming an Ir(CO) interfacial site. This facilitates O_2 activation between Ir and aluminum from the support. They observed that the reaction barrier is reduced between gas-phase CO and adsorbed O in Ir(CO)(O) *via* an Eley–Rideal mechanism.[40]

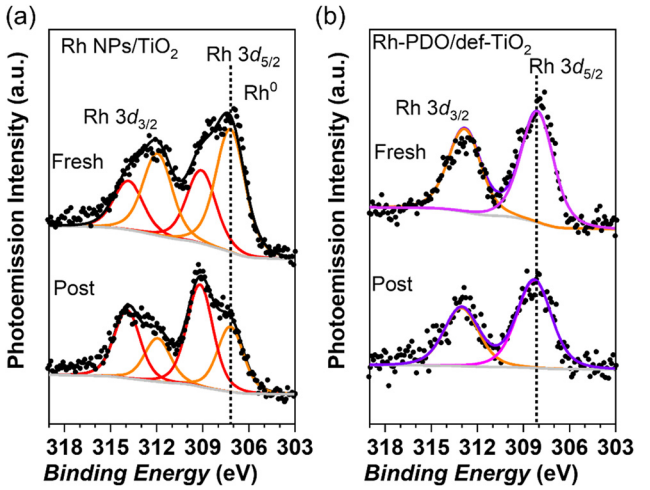

Fig. 11 XP spectra of Rh 3d for (a) Rh NPs/TiO_2, and (b) Rh–PDO/def-TiO_2 as fresh catalysts (top curves) and post-reaction catalysts (bottom curves). For Rh NPs (a), two species are identified: Rh^0 at a binding energy of 307. 2 eV for Rh 3 $d_{5/2}$ (vertical dashed line) and Rh^{3+}. For Rh–PDO (b), the data fit well with a single component, Rh^{2+}, at a binding energy of 308.2 eV (vertical line).

For Rh–PDO/def-TiO_2 and Rh NPs/TiO_2, we propose a Langmuir–Hinshelwood (L–H) mechanism. In the former, the reaction occurs without carbonate formation, possibly due to the rapid desorption of the generated CO_2 from the defective TiO_2 surface.

3.7 Characterization of ligand-coordinated single site Rh catalysts after reaction

The post-reaction catalysts were analyzed using XPS (Fig. 11 and S8†), EXAFS (Fig. S9†), and DRIFTS (Fig. S3†). For Rh–PDO on defective TiO_2, the Rh 3d spectrum showed virtually no change in binding energy after the CO oxidation reaction (Fig. 11b). The Rh 3d spectra (Fig. 11a) for Rh NPs show that the Rh species are oxidized after the reaction. XPS and DRIFTS measurements confirm the presence of the ligand before and after the reaction (Fig. S3 and S8†). In EXAFS measurements, the N (Rh–O/N) and N (Rh–Cl) for both Rh–PDO catalysts do not change significantly after the reaction (Table S2†). The Rh–Rh shell contribution decreases in the EXAFS spectrum for Rh NPs after the CO oxidation reaction. After fitting the spectra, we found that N (Rh–Rh) drops from 1.7 ± 0.9 to 1.2 ± 0.7, while N (Rh–O) increases from 5.2 ± 0.4 to 5.5 ± 0.3.

4. Conclusion

Rh–ligand coordinated single atom catalysts have been successfully synthesized, demonstrating enhanced catalytic activity for the CO oxidation reaction at relatively low temperatures. The use of a defective TiO_2 surface as the support affects the configuration of Rh with the ligand,

resulting in a different reaction pathway for CO oxidation compared to Rh–ligand on a pristine TiO_2 surface. Additionally, the ligand coordinated single site Rh catalyst exhibits high stability in an oxygen-rich environment, preventing the formation of carbonate-like species during the reaction. This behavior makes these catalysts promising for applications such as CO removal in controlling automobile emissions and in hydrogen fuel cell technologies.

Data availability

The authors declare that the data supporting the findings of this study are available within the paper and its ESI† files. Should any raw data files be needed in another format they are available from the corresponding author upon reasonable request.

Conflicts of interest

There are no conflicts to declare.

Acknowledgements

This work was supported by the U. S. Department of Energy, Office of Basic Energy Sciences, Chemical Sciences program, DE-SC0021390. XPS measurements were carried out at the Indiana University (IU) Nanoscale Characterization Facility, with assistance from Dr. Yaroslav Lasovyj. Scanning transmission electron microscopy (STEM) and EDS measurements were performed at the IU Electron Microscopy Center, operated by Dr. Xun Zhan and Dr. Jun Chen. XAS measurements were performed at beamline 20-BM at the Advanced Photon Source, an Office of Science User Facility operated for the U.S. Department of Energy (DOE) Office of Science by Argonne National Laboratory, under Contract No. DE-AC02-06CH11357. ICP-MS measurements were performed in the IU Department of Earth and Atmospheric Sciences by Dr. Shelby Rader.

References

1 M. Haruta, S. Tsubota, T. Kobayashi, H. Kageyama, M. J. Genet and B. Delmon, *J. Catal.*, 1993, **144**, 175–192.
2 T. Kropp, Z. Lu, Z. Li, Y.-H. C. Chin and M. Mavrikakis, *ACS Catal.*, 2019, **9**, 1595–1604.
3 H. Xu, C.-Q. Xu, D. Cheng and J. Li, *Catal. Sci. Technol.*, 2017, **7**, 5860–5871.
4 X. Liu, M. Xu, L. Wan, H. Zhu, K. Yao, R. Linguerri, G. Chambaud, Y. Han and C. Meng, *ACS Catal.*, 2020, **10**, 3084–3093.
5 S. Bonanni, K. Ait-Mansour, W. Harbich and H. Brune, *J. Am. Chem. Soc.*, 2012, **134**, 3445–3450.
6 A. D. Allian, K. Takanabe, K. L. Fujdala, X. Hao, T. J. Truex, J. Cai, C. Buda, M. Neurock and E. Iglesia, *J. Am. Chem. Soc.*, 2011, **133**, 4498–4517.
7 B. Qiao, A. Wang, X. Yang, L. F. Allard, Z. Jiang, Y. Cui, J. Liu, J. Li and T. Zhang, *Nat. Chem.*, 2011, **3**, 634–641.
8 K. Ding, A. Gulec, A. M. Johnson, N. M. Schweitzer, G. D. Stucky, L. D. Marks and P. C. Stair, *Science*, 2015, **350**, 189–192.
9 H. Guan, J. Lin, B. Qiao, X. Yang, L. Li, S. Miao, J. Liu, A. Wang, X. Wang and T. Zhang, *Angew. Chem., Int. Ed.*, 2016, **55**, 2820–2824.
10 B. Han, T. Li, J. Zhang, C. Zeng, H. Matsumoto, Y. Su, B. Qiao and T. Zhang, *Chem. Commun.*, 2020, **56**, 4870–4873.
11 S. J. Tauster, S. C. Fung, R. T. K. Baker and J. A. Horsley, *Science*, 1981, **211**, 1121–1125.
12 S. J. Tauster, S. C. Fung and R. L. Garten, *J. Am. Chem. Soc.*, 1978, **100**, 170–175.
13 X. Zhou, L. Chen, G. E. Sterbinsky, D. Mukherjee, R. R. Unocic and S. L. Tait, *Catal. Sci. Technol.*, 2020, **10**, 3353–3365.
14 F. Jiang, L. Zeng, S. Li, G. Liu, S. Wang and J. Gong, *ACS Catal.*, 2015, **5**, 438–447.
15 J. Wan, W. Chen, C. Jia, L. Zheng, J. Dong, X. Zheng, Y. Wang, W. Yan, C. Chen, Q. Peng, D. Wang and Y. Li, *Adv. Mater.*, 2018, **30**, 1705369.
16 N. J. O'Connor, A. S. M. Jonayat, M. J. Janik and T. P. Senftle, *Nat. Catal.*, 2018, **1**, 531–539.
17 M. J. Hülsey, B. Zhang, Z. Ma, H. Asakura, D. A. Do, W. Chen, T. Tanaka, P. Zhang, Z. Wu and N. Yan, *Nat. Commun.*, 2019, **10**, 1330.
18 R. M. Al Soubaihi, K. M. Saoud and J. Dutta, *Catalysts*, 2018, **8**, 660.
19 S. Dey, G. C. Dhal, D. Mohan and R. Prasad, *Adv. Compos. Hybrid Mater.*, 2019, **2**, 626–656.
20 L. Chen, G. E. Sterbinsky and S. L. Tait, *J. Catal.*, 2018, **365**, 303–312.
21 L. Chen, I. S. Ali, G. E. Sterbinsky, X. Zhou, E. Wasim and S. L. Tait, *Catal. Sci. Technol.*, 2021, **11**, 2081–2093.
22 B. Ravel and M. Newville, *J. Synchrotron Radiat.*, 2005, **12**, 537–541.
23 L. S. Kibis, A. I. Stadnichenko, S. V. Koscheev, V. I. Zaikovskii and A. I. Boronin, *J. Phys. Chem. C*, 2016, **120**, 19142–19150.
24 L. Óvári and J. Kiss, *Appl. Surf. Sci.*, 2006, **252**, 8624–8629.
25 J. Evans, B. Hayden, F. Mosselmans and A. Murray, *J. Am. Chem. Soc.*, 1992, **114**, 6912–6913.
26 E. Ivanova, M. Mihaylov, F. Thibault-Starzyk, M. Daturi and K. Hadjiivanov, *J. Catal.*, 2005, **236**, 168–171.
27 R. Lang, T. Li, D. Matsumura, S. Miao, Y. Ren, Y.-T. Cui, Y. Tan, B. Qiao, L. Li, A. Wang, X. Wang and T. Zhang, *Angew. Chem., Int. Ed.*, 2016, **55**, 16054–16058.
28 J. C. Matsubu, V. N. Yang and P. Christopher, *J. Am. Chem. Soc.*, 2015, **137**, 3076–3084.
29 S. Tauster, S. Fung and R. L. Garten, *J. Am. Chem. Soc.*, 1978, **100**, 170–175.
30 S. Yokota, K. Okumura and M. Niwa, *Catal. Lett.*, 2002, **84**, 131–134.
31 M. A. Newton, S. G. Fiddy, G. Guilera, B. Jyoti and J. Evans, *Chem. Commun.*, 2005, 118–120.
32 J.-D. Grunwaldt, L. Basini and B. S. Clausen, *J. Catal.*, 2001, **200**, 321–329.

33 Y. Tang, C. Asokan, M. Xu, G. W. Graham, X. Pan, P. Christopher, J. Li and P. Sautet, *Nat. Commun.*, 2019, **10**, 4488.
34 M. S. Chen, Y. Cai, Z. Yan, K. K. Gath, S. Axnanda and D. W. Goodman, *Surf. Sci.*, 2007, **601**, 5326–5331.
35 Y. Zhou, D. E. Doronkin, M. Chen, S. Wei and J.-D. Grunwaldt, *ACS Catal.*, 2016, **6**, 7799–7809.
36 E. A. Wovchko and J. T. Yates, *J. Am. Chem. Soc.*, 1998, **120**, 10523–10527.
37 L. F. Liao, C. F. Lien, D. L. Shieh, M. T. Chen and J. L. Lin, *J. Phys. Chem. B*, 2002, **106**, 11240–11245.
38 L. Mino, G. Spoto and A. M. Ferrari, *J. Phys. Chem. C*, 2014, **118**, 25016–25026.
39 Y. Zhu, D. Liu and M. Meng, *Chem. Commun.*, 2014, **50**, 6049–6051.
40 Y. Lu, J. Wang, L. Yu, L. Kovarik, X. Zhang, A. S. Hoffman, A. Gallo, S. R. Bare, D. Sokaras, T. Kroll, V. Dagle, H. Xin and A. M. Karim, *Nat. Catal.*, 2019, **2**, 149–156.
41 H. Wang, J.-X. Liu, L. F. Allard, S. Lee, J. Liu, H. Li, J. Wang, J. Wang, S. H. Oh, W. Li, M. Flytzani-Stephanopoulos, M. Shen, B. R. Goldsmith and M. Yang, *Nat. Commun.*, 2019, **10**, 3808.
42 J. Xu, Y. Wang, K. Wang, M. Zhao, R. Zhang, W. Cui, L. Liu, M. S. Bootharaju, J. H. Kim and T. Hyeon, *Angew. Chem., Int. Ed.*, 2023, **62**, e202302877.